DESIGN AND OPTIMIZATION OF A COMPACT LOW-COST OPTICAL PARTICLE SIZER

Tomas Njalsson

A thesis

submitted in partial fulfillment of the

requirements for the degree of

Master of Science in Mechanical Engineering

University of Washington

2016

Reading Committee:

Igor V. Novosselov, Chair

Jonathan Posner

Edmund Seto

Program Authorized to Offer Degree:
Department of Mechanical Engineering

University of Washington

Abstract

DESIGN AND OPTIMIZATION OF A COMPACT LOW-COST OPTICAL PARTICLE SIZER

Tomas Njalsson

Chair of the Supervisory Committee:
Igor V. Novosselov
Department of Mechanical Engineering

Determining particulate matter (PM) concentrations in ambient air is of major importance in applications of aerosol research; personal exposure assessments, industrial particle monitoring, and air quality studies. Optical particle counters (OPCs) measure the elastic light scattering of individual particles and provide time and size-resolved PM number concentrations. They are common due to their simplicity and low-cost. However, many of them suffer from non-monotonic size dependence of scattered light intensity and its variability with changing the complex refractive index (CRI) of particles. This weakness is particularly common in portable low-cost OPCs.

This contribution describes the process of designing, validating, and testing an OPC for size measurements of aerosols. The proposed device is characterized by four main principles; low sensitivity to variations in the CRI of particles, accurate sizing, compactness, and low-cost. The design utilizes small form factor low-cost components (total cost < $100) and measures less than 45 x 25 x 15mm (L, W, H) in size. An optimization methodology is defined and used to determine the optimal angular range for collection of scattered light. An adjustable experimental

setup was used to validate the numerical findings and to test the performance of the optimized angular range in comparison to two equally sized angular ranges, commonly employed in OPCs. The experiments used six different spherical monodisperse particles of known size and CRI; PSL (n = 1.61), alumina (n = 1.78), and silica (n = 1.53); 2 and 4 μm in diameter. The PSL particles were used for calibration before the device was exposed to particles with different CRIs. The experimental response was in good agreement with the numerical calculations overall. The average sizing error was 6.87% for the optimal angular range, compared to 32.21% and 25.45% for the alternatives. The results show clearly that the optimal angular range is effective in eliminating the ambiguity that is commonly present when OPCs are used in the field. The findings were consistent across the two sizes and all CRIs.

TABLE OF CONTENTS

LIST OF FIGURES

LIST OF TABLES

ACKNOWLEDGEMENTS

Foremost, I would like to express my sincere gratitude to my advisor Prof. Igor V. Novosselov for his continuous support of my study and research, for his patience, motivation, enthusiasm, and immense knowledge. I could not have imagined having a better advisor and mentor for my Master's study.

Besides my advisor, I would like to thank the rest of my thesis committee: Prof. Edmund Seto, and Prof. Jonathan Posner, for their comments and questions.

I would like to thank my co-researcher Emily Roach for her contribution to this body of research.

A special note of thanks to all my co-workers in the NRG Lab.

Last but not least, I would like to thank my family and friends.

This research was funded in part by a grant from the NIH National Institute of Biomedical Imaging and Bioengineering (U01 EB021923).

CHAPTER 1: INTRODUCTION

Quantifying personal exposure to particulate matter (PM) is an important part of health risk assessment for individuals. Exposure to PM is associated with multiple adverse health effects including cardiovascular disease, cardiopulmonary disease, and lung cancer [1-7]. Estimates show that approximately 3% of cardiopulmonary and 5% of lung cancer deaths are attributed to PM exposure globally, with recent studies indicating that the effects on mortality might be even higher [8]. The health and environmental research communities have standardized three categories of PM as its primary interest, particles smaller than 1 μm (PM_1, submicron particles), particles smaller than 2.5 μm ($PM_{2.5}$, fine particles), and particles smaller than 10 μm (PM_{10}). Studies have evidenced how particle deposition in the human respiratory tract and the resultant adverse health effects depend on the size distribution of particles [9, 10]. Additionally, PM concentrations and distributions are known to vary significantly in both space and time [11, 12]. Hence, time and size-resolved PM measurements are more informative than traditional total PM weight measurements when assessing negative effects on human health.

The U.S. Environmental Protection Agency (EPA) and the EU have adopted the PM_{10} and $PM_{2.5}$ criteria for monitoring ambient air quality [13, 14]. However, the density of monitoring sites varies widely across the globe making annual exposure estimations a challenge [15]. The EPA has established cumulative methods to measure size-resolved mass concentrations of PM [16]. The methods include gravimetric filters and cascade impactors, both of which provide gravimetric and chemical PM information after their respective samples have been processed carefully. These methods are highly accurate and precise, but they do not provide temporal information. Additionally, cumulative methods are generally labor-intensive and time-consuming which severely limits their practicality. With regard to personal exposure assessments, cumulative

methods lack the space-time resolution to clearly pinpoint locations and timings of high PM exposure. Instruments that use gravimetric filters and cascade impactors are usually not portable, which limits their usability for exposure and epidemiology oriented studies.

Several different methods enable automatic measurements of size and time-resolved PM concentrations. Various instruments are now available that use these methods to provide real-time PM mass concentrations indirectly by measuring PM number concentrations. The most commonly used instruments are based on light scattering and aerodynamic methods. The respective instruments measure size and time-resolved PM number concentrations directly and infer size and time-resolved mass concentrations by making the appropriate particle density assumptions. Accurate instruments that use aerodynamic methods are generally expensive and not portable, making them impractical for exposure assessments and mass deployments. Light scattering instruments are more commonly used, particularly when measuring particles in the 0.1 to 10 μm range, as they are simpler, less expensive, and increasingly smaller than the alternatives. Small sensors that measure bulk light scatter of multiple particles simultaneously are referred to as particle sensors, while devices that measure the light scatter of individual particles are called optical particle counters (OPCs). The development of OPCs over the last half century has provided them with more accurate particle sizing capabilities, rendering the "counter" terminology unfitting. The acronym OPC is used in this contribution for counters, spectrometers, and sizers, regardless of their sizing capabilities. Particle sensors gauge the bulk number of particles in the air, by essentially measuring the opacity of air, and can be calibrated to provide indications of mass concentrations. They are compact, low-cost, can be integrated into handheld devices, and have been used in large scale PM exposure studies [17]. In contrast, OPCs count individual particles and provide more accurate size-resolved profiles of PM number concentrations with proper

calibration. In comparison to particle sensors, they are more complex, expensive, and often larger due to the additional hardware components they require.

Irrespective of their exact definition, most light scattering devices rely on the same physical principle; the elastic scattering of light. They measure the light scattered by particles and determine the size of each particle based on the measured intensity of the scattered light. Therefore, they all suffer from the same crucial weakness related to the scattered light intensity; the measured scattered light intensity is very sensitive to small variations in the complex refractive index (CRI) of particles, and the scattered light intensity displays non-monotonic size dependence for certain particle sizes and CRIs. This problem creates an ambiguity when it comes to sizing particles of varied and unknown CRIs; a scenario that is frequent in environmental PM monitoring and personal exposure assessments. Hence, the accuracy of the measured size distribution hinges on the knowledge of the true CRI of each individual particle, which is difficult to determine. This ambiguity can lead to substantial errors in the retrieved PM number concentration. The error is further amplified if the number concentration is converted to mass concentration, i.e. the measured diameter is cubed in order to calculate the volume, resulting in information that can differ significantly from reality. The CRI sensitivity is particularly apparent in compact low-cost devices. A recent study found that very low-cost (<$100) particle sensors consistently provided erroneous number concentrations when they were exposed to particles that differed from the calibration particles [18]. Another study evaluated three commercially available low-cost particle sensors, the results show that all three sensors depended highly on particle composition and size, providing measurements with an error of up to 1000% [19]. Measurements obtained using low-cost sensors have also been found to suffer from sensor-to-sensor variability due to lack of quality control and the differences in the individual components in these sensors [18, 20].

Researchers have addressed the CRI sensitivity problem by designing OPCs that measure scattered light at multiple different angles simultaneously [21], or by employing dual wavelength techniques [22]. However, these solutions involve complex and expensive components unsuitable for compact low-cost devices. A common workaround to enable the use of low-cost OPCs or particle sensors is to use sequential sampling systems to collect the particles on a filter after they have been measured by the OPC. The filters are then analyzed afterward in laboratories to determine their average CRI, which is used to post-calibrate the OPC data. Despite the potential, there are drawbacks with using this method to obtain accurate data. Retrieving the average values is a non-automated, expensive, and labor-intensive task which eliminates the benefits of using a compact low-cost device. There is a clear need for compact low-cost devices that are less sensitive to the weaknesses previously outlined. These weaknesses are detrimental to the usability of the compact low-cost devices available today. An ideal device would be low-cost and come in a small form factor while providing accurate time and size-resolved PM measurements, unaffected by variations in the CRI of particles.

This contribution describes the process of designing, validating, and testing an OPC for size measurements of aerosols. The proposed device is characterized by four main principles; low sensitivity to variations in the CRI of particles, accurate sizing, compactness, and low-cost. The design utilizes small form factor inexpensive components (total device cost < $100) and measures less than 45 x 25 x 15mm (L, W, H) in size. A novel optimization methodology is defined and used to optimize the internal scattering geometry of the device; minimizing both the sensitivity towards CRI variations and other characteristics that negatively affect the sizing accuracy. The proposed OPC is designed for applications where particle sensors have traditionally been used; e.g. in real-time personal exposure assessment scenarios, monitoring HVAC systems, and general

air quality management. The thesis is organized as follows: (i) the angular dependence of scattered light is analyzed, (ii) an optimization scheme based on the elastic light scattering of spherical homogeneous particles (Mie theory) is constructed and used to determine the optimal scattering geometry for the proposed device. (iii) The optimal scattering geometry is numerically compared to two alternative light scattering geometries that are common in commercially available OPCs (perpendicular and near-forward scattering). (iv) An experimental setup utilizing small form factor low-cost components is used to validate the numerical findings and to evaluate the performance of the OPC in comparison to the two alternatives.

CHAPTER 2: APPROACH

2.1 THEORETICAL BACKGROUND

The basic principle of OPCs is to detect and measure the intensity of light scattered by individual particles as they traverse a focused beam of light. A portion of the scattered light is collected and directed to a photodetector, which converts the scattered light into a voltage pulse. Thereby, each particle generates a pulse, whose amplitude depends on the particle's diameter, CRI, shape, and surface roughness. An ideal OPC has a monotonic relationship between the particle diameter and the measured light intensity, independent of the particle's CRI, shape, and surface roughness, providing distinctive particle sizing. However, even for the ideal case of homogeneous spherical particles, uncertainties in the knowledge of the CRI can lead to significant errors in the retrieved size distribution.

The spatial distribution of light scattered by spherical particles can be calculated directly with Mie theory, a solution to Maxwell's equations in the form of an infinite series of spherical multipole partial waves [23, 24]. The spatial distribution is described with the polar scattering in the scattering plane, containing the particle and the incident light beam, and the azimuthal scattering around the axis of the incident light beam. For a linearly polarized light beam irradiating a particle from one direction, the OPC response, R, is given by Equation 2.

$$R = \frac{\lambda^2}{4\pi^2} \int_{\phi_1}^{\phi_2} \int_{\theta_1}^{\theta_2} G(x,m,\theta,\phi)\left(I_{hor}(x,m,\theta,\phi) + I_{ver}(x,m,\theta,\phi)\right)d\theta d\phi \quad (2)$$

Where G represents characteristics specific to each device (amplification, signal processing, stray light), I_{hor} and I_{ver} are the scattered light intensities polarized horizontal and vertical to the plane of the incoming plane wave, $m = n - ik$ is the CRI of the particle, $x = \frac{\pi d}{\lambda}$ is the dimensionless particle size parameter where d is the particle's diameter and λ is the wavelength of the incoming

light. If the particle is assumed to be spherical and homogeneous, the two intensities, I_{hor} and I_{ver} can be calculated with Mie theory. The location of the photodetector that measures the scattered light is represented by θ and ϕ, the angles that limit the solid angle in which the scattered light is collected. Figure 1 displays the typical wave-matter interaction that occurs in light scattering devices.

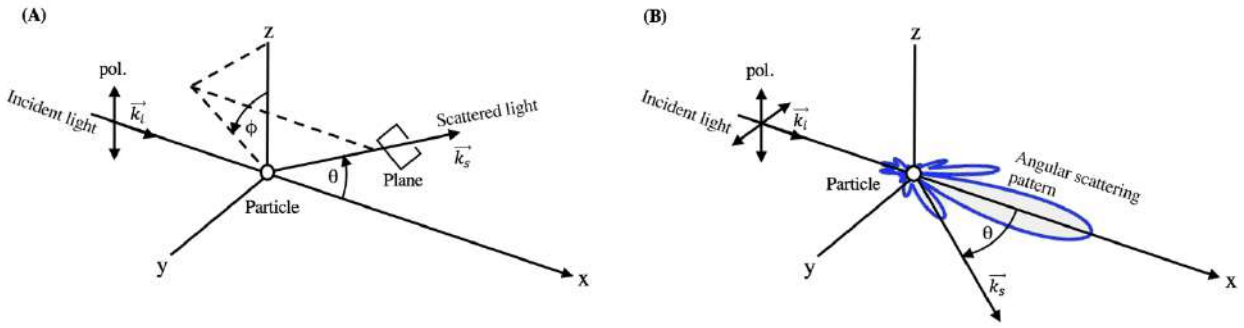

Figure 1: (A) Scattering geometry for an incident beam of light propagating along the positive x-axis. The direction of the light is defined by the incident wave vector $\vec{k_i}$, and the polarization (pol.) of the light is in the vertical z-direction. The light scatters from the spherical particle to the photodetector (plane) in the direction of the scattering wave vector $\vec{k_s}$. The polarization of the scattered light will be in the direction of the projection of the incident polarization onto the plane. (B) Using an identical scattering geometry with ϕ = 90° fixed and a linearly polarized incident light source simplifies the problem. The angular scattering pattern (blue) becomes a function of θ only, with the scattering being isotropic in other planes and symmetric relative to the x-axis.

The scattering geometry in Figure 1B shows an isotropic angular scattering pattern (colored blue) for a 1 μm particle with a CRI of m = 1.5 - 0i, calculated using Mie theory with a fixed azimuthal angle ϕ = 90°. Figure 2 shows the angular scattering pattern for the same scattering geometry as a function of θ, for different sizes and CRI. The scattered light intensity is angularly dependent, as observed in Figure 2. Most angles display oscillatory behavior, but by integrating over specific angular ranges the intensity, and hence the response, can be smoothed. Non-monotonic size dependence is apparent in Figure 2 (Left) for certain angles, smaller particles may scatter more or

less light than larger particles of the same type, leading to multivaluedness in the response of the OPC. This is particularly evident in the range around θ = 20° and θ > 100°. Figure 2 (Right) shows the scattering intensity for a fixed 1 μm particle as a function of angle and CRI. The scattered light intensity shows substantial variance despite the particle size being fixed, it ranges erratically and displays little to no relation to the increase or decrease in CRI. These two effects, the non-monotonic size dependence and the deviations brought by variations in the CRI of particles, make unique particle sizing difficult.

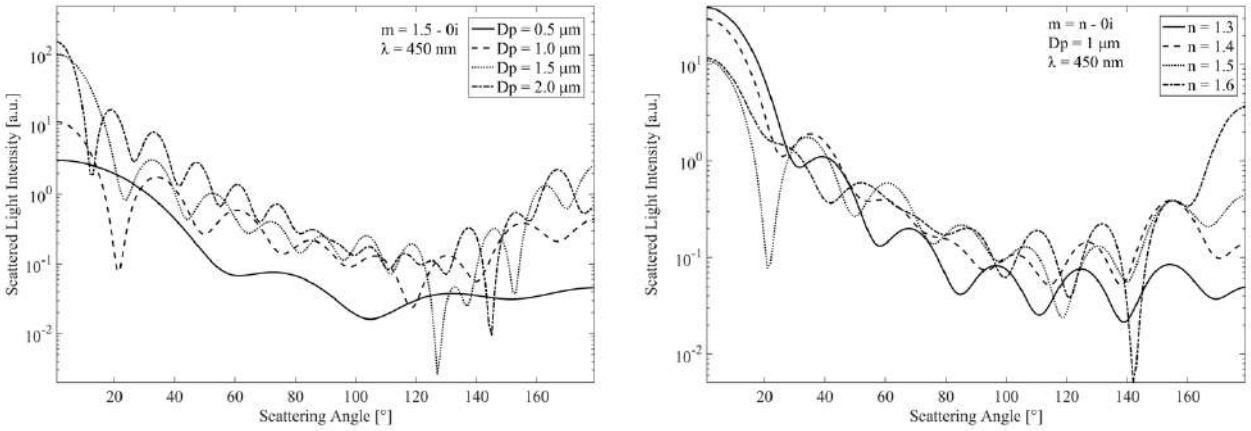

Figure 2: Scattered light intensity as a function of scattering angle for a linearly (vertically) polarized light source. (Left) Four different particle sizes ranging from 0.5 to 2.0 μm with a constant CRI. (Right) Four different particle CRIs ranging from 1.3-0i to 1.6-0i with a constant particle diameter of 1 μm.

The response of any OPC is proportional to the scattered light intensity they measure. More strictly, it is a function of the parameters in Equation 2; the integrated angular range which represents the collection area of the photodetector, the wavelength and polarization of the incident light beam, and the optical properties, shape and surface roughness of the measured particles. In general, all angles and scattering geometries have their own characteristics which may or may not be favorable for certain purposes. Previous studies have suggested that that near-forward scattering (θ = 5-25°) of light by particles is less sensitive to CRI [21], this angular range is often referred to

as the Mie Lobe and contains mostly diffracted light that is less affected by variations in CRI. Another angular range commonly used in OPCs is perpendicular scattering, an angular range that is centered at $\theta = 90°$. The perpendicular positioning of the photodetector limits the effects of stray light inside the device, it is simple to manufacture, and has traditionally been the most commonly used angular range in OPCs [25].

In addition to the sizing accuracy considerations, there are other important factors that have to be accounted for in the design process of every OPC. The scattered light intensity generally increases as the angle is closer to $\theta = 0°$, thereby increasing the device' capabilities of measuring smaller particles; i.e. the limit of detection (LOD). The LOD is defined as the smallest measured particle size that provides a S/N ratio of 10, where the signal is the amplitude of the measured pulse and the noise is the standard deviation of the response without any particles inside the device (background noise). Not only is the value of the intensity important, but also its range. The dynamic range of the OPC is defined as the ratio of the highest measured intensity over the lowest, a ratio that varies substantially for different angles. A large dynamic range requires more powerful electronics in the OPC and constrains the range of measurable particle sizes. A high LOD (the smallest detectable particle is larger) limits the lower end of the targeted size range and requires a high amplification, further complicating the electronics used in the device.

2.2 OPTIMIZATION SCHEME

Instead of heuristically examining multiple angular ranges to assess their capabilities, our approach is to build a simple optimization scheme to find the optimal angular range for this device. In the development of the optimization scheme, the strong angular dependence of the scattered light is used to find an angular range that minimizes the following four unfavorable characteristics: sensitivity towards CRI, non-monotonic size dependence, the dynamic range of the response, and the LOD. Together, they form the optimization criteria. The optimization scheme uses Mie theory to calculate the response characteristics of each and every angular range, to determine the optimized angular range for light collection (photodetector position). The resulting problem is a multi-objective optimization with a Pareto set of multiple equally optimal solutions. In order to approach a single solution, each criterion is normalized and assigned a weight in the range from zero to unity of increased importance. Thereby, the scheme can find the optimal angular range using the appropriately weighted criteria. The measure of each criterion must be independent of the other criteria; the approach taken here is to quantify each criterion mathematically in a way that isolates the respective error source. Table 1 displays an overview of the criteria. Minimizing the CRI sensitivity is essential and is assigned a weight of unity, it is quantified as the Coefficient of Variation (CV), the ratio of the standard deviation to the mean, as a function of particle size where the CRI is varied. The monotonicity of the response impacts the sizing accuracy of the device and is assigned a weight of unity. It is quantified as the number of multivalued instances for all particle sizes and types in the range considered, a pseudocode is shown in Table 1. The dynamic range is assigned a lower weight because it can be compensated by choosing fitting electronics. The LOD criterion is assigned a weight of one-half, and while it is essential for the

performance of the proposed device, the calculated LOD will be lower than the realized LOD since it is heavily affected and limited by the electrical and optical components used.

Table 1: Optimization criteria and constraints

Criterion	Description	Pseudocode	Weight
CRI Sensitivity	Coefficient of Variation	$\frac{\sigma(R(d_{i,\text{CRI varied}}))}{\mu(R(d_{i,\text{CRI varied}}))}$	1
Monotonicity	Instances of multivaluedness	for i = 1 to end: $R(d_i)<\text{any}(R(d_{i-1,\ i-2,..}))$	1
Dynamic Range	Response range	$\frac{\max(R)}{\min(R)}$	0.3
LOD	Scattering intensity of 0.1 μm particle	$R(D_{\text{smallest}})$	0.5

Constraint	Value
Particle diameter	0.1 to 10 μm
RI – Real Part	1.3 to 2.0
RI – Imag. Part	0 to 0.1
Max Angle	20°
Angular range	5 to 175°
Particle shape	Spherical
Polarization	Linear

The constraints listed in Table 1 are chosen based on the targeted application for this device, monitoring size-resolved PM concentrations in urban and rural environments. The most common particles found in these environments range from organic particles to weakly absorbing particles. One study found that urban aerosols have an average CRI of 1.56-i0.08 [26]. Another study reported on PM around the city of Paris and found the average CRI to be 1.51-i0.017 [27]. A similar conclusion is found in other sources [28]. Evidently, the real part of the refractive index ranges from 1.3 to 2.0 for individual particles with 1.5 to 1.6 being the average, while the complex part ranges from almost zero in rural areas to 0.1 in more urban areas due to increased black carbon concentrations. To summarize, the range of particles chosen for the optimization in this study are non- and weakly absorbing spherical particles with a diameter from 0.1 to 10 μm and a CRI ($m = n - ik$) in the range $n = 1.3$ to 2.0 and $k = 0$ to 0.1. Several other factors constrain the optimization, mainly stemming from the physical design of the device: its small formal factor and

low-cost. The angular range that the scheme considers is limited to 5 - 175° (with the scattering being symmetric relative to the direction of the light) to account for the location of the laser source and the laser dump, and the maximum angle that the photodetector can cover is 20° due to size constraints and the absence of collection optics. The polarization of the incident light source is assumed to be linear (horizontal or vertical) on the grounds that laser diodes are linearly polarized. The selected optimization criteria, constraints, and their relative weight in this work are meant to represent the respective application that the device is designed for, other constraints and weighting selections are possible and will surely result in a different outcome.

2.3 DETERMINING THE OPTIMAL PHOTODETECTOR POSITION

The optimization scheme uses Mie theory to determine the response characteristics of every scattering geometry and angular range; they are then ranked using the appropriately weighted criteria. After calculating all possible combinations, the angular range from 38° to 58° in the x-y plane was found to be the best performer given the chosen constraints and inputs. The following analysis includes two alternative angular ranges, commonly used in commercially available OPCs. In total, the analysis includes three equally sized angular ranges, the optimal range (38-58°), the perpendicular range (80-100°) and near-forward range (5-25°).

Figure 3 displays the simulated scattered light intensity as a function of particle diameter for the optimized angular range in comparison to the near-forward and perpendicular angular ranges, where each of the eight lines represents a specific CRI ranging from 1.3-0i to 2.0-0i. The scattered light intensity increases as the angular range gets closer to the forward scattering Mie lobe; the near-forward range has the highest scattering intensity overall. The variance of the optimized range is the smallest, particularly for particles larger than 1 μm, which indicates that it should be more capable of correctly sizing particles with an unknown CRI. The perpendicular range displays high sensitivity to variations in CRI for all particle sizes, while the near-forward range is the most sensitive when smaller particles are considered. Figure 4 shows the CV as a function of particle diameter for the three angular ranges; the CV was previously defined as a measure of CRI sensitivity. Evidently, the optimized angular range is least sensitive to variations in CRI out of the three, with the effect being more pronounced for particles larger than 1 μm. The near-forward angular range also displays a low CV overall, with the exception of particles smaller than 1 μm. The perpendicular angular range has the highest CV overall, but the lowest for particles smaller than 1 μm.

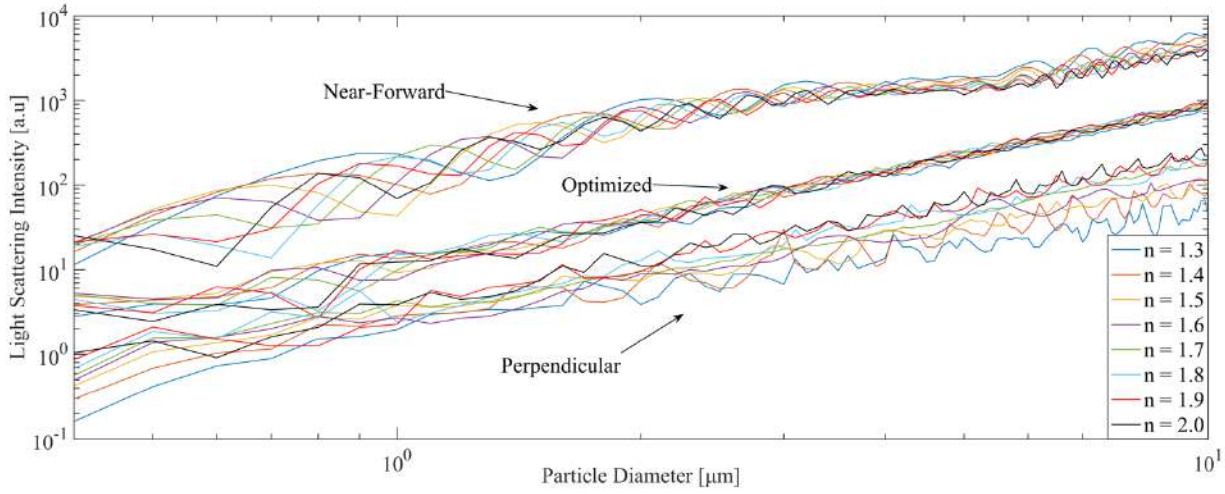

Figure 3: Simulated scattered light intensity for the near-forward, optimized and perpendicular angular ranges, calculated with Mie theory. The particle diameter ranges from 0.1 to 10 μm and the refractive index ranges from 1.3-0i to 2.0-0i. Both axes are logarithmic.

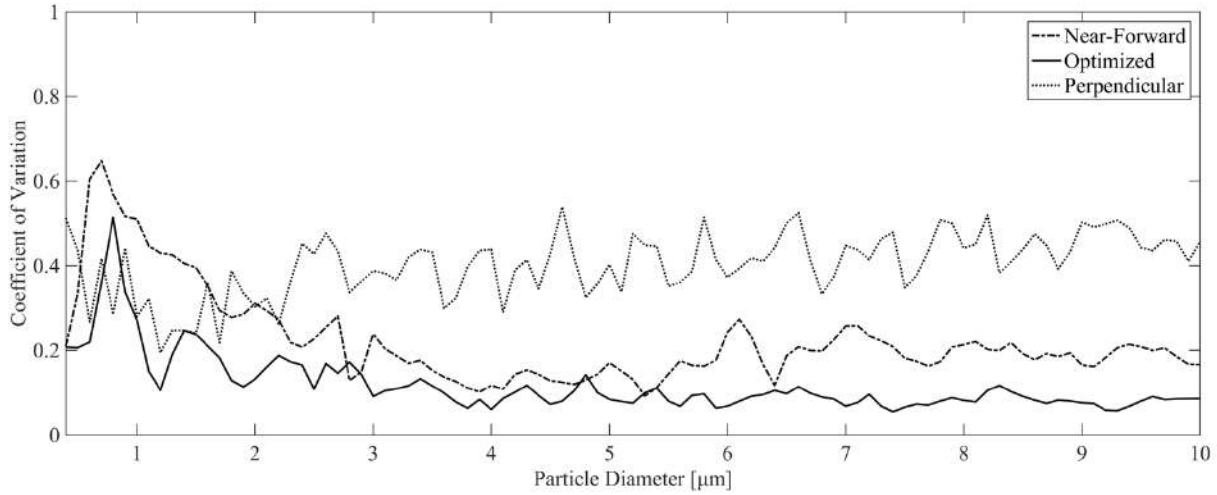

Figure 4: Coefficient of Variation (CV) for the near-forward, optimized and perpendicular angular ranges. The particle diameter ranges from 0.1 to 10 μm and the refractive index ranges from 1.3-0i to 2.0-0i.

The purpose of the optimization scheme was to minimize unfavorable characteristics that increased sizing error. This sizing error is quantified here as the Relative Sizing Error (RSE) and it is used as the basis to compare the performance of the optimized angular range to the two alternative ranges. RSE as a measure incorporates multiple error sources into one variable, namely the CRI

sensitivity and the monotonicity of the response. Equation 3 defines the RSE, it is the ratio of the difference between the actual diameter and the retrieved diameter over the actual diameter.

$$RSE = \frac{d_{retrieved} - d_{actual}}{d_{actual}} \quad (3)$$

The simulated RSE is displayed in Figure 5 and Figure 6 for non-absorbing and weakly-absorbing particles respectively. The figures are generated using Mie theory simulations where each angular range sizes thousands of different spherical particles ranging in size and CRI. The resulting RSE is calculated for each particle and the normalized total is displayed in the figures as a histogram. The RSE figures show both the frequency of erroneous sizing and the extent of it.

While all three angular ranges show behavior of sizing error, the error is the smallest for the optimized range. The optimized range sizes particles with zero error 30% and 20% of the time for non-absorbing and weakly absorbing particles, the other two angular ranges size particles with zero error 15% and 10% of the time. Figure 7 and Figure 8 show the RSE as a function of particle diameter. The RSE is dependent on the particle diameter for both the near-forward and the perpendicular angular ranges. The near-forward range over sizes particles smaller than 4 μm while larger particles are undersized. The perpendicular range generally over sizes particles with a trend towards under sizing with increased size. In comparison, the optimized range displays more of a systematic bias towards under sizing with an exception for particles smaller than 0.5 μm which are oversized. Although the figures display simulated results that do not mirror real-world situations, they indicate that the optimized angular range could be more effective in correctly sizing particles overall.

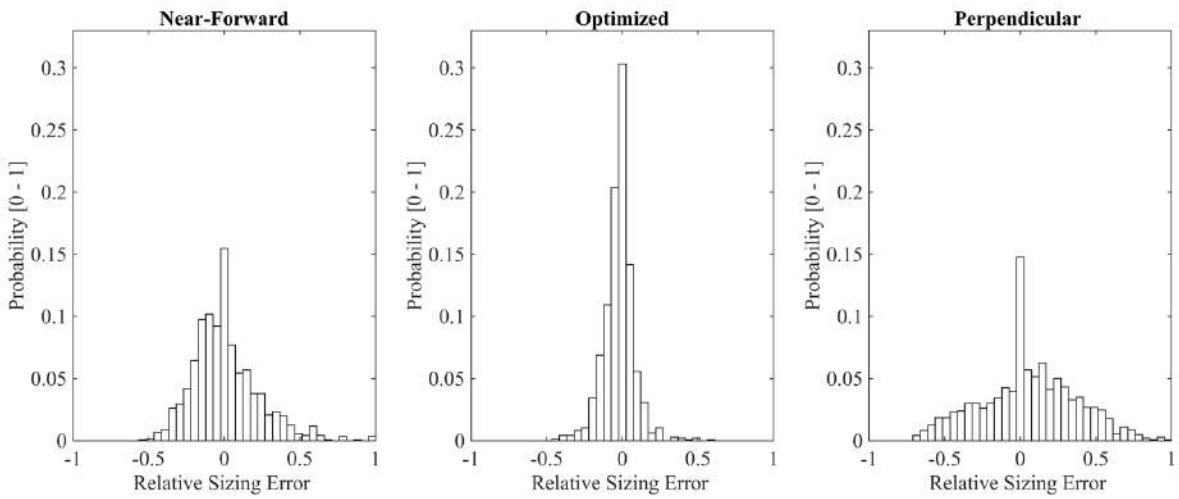

Figure 5: Simulated RSE distribution for non-absorbing particles in the range 0.1 to 10 μm.

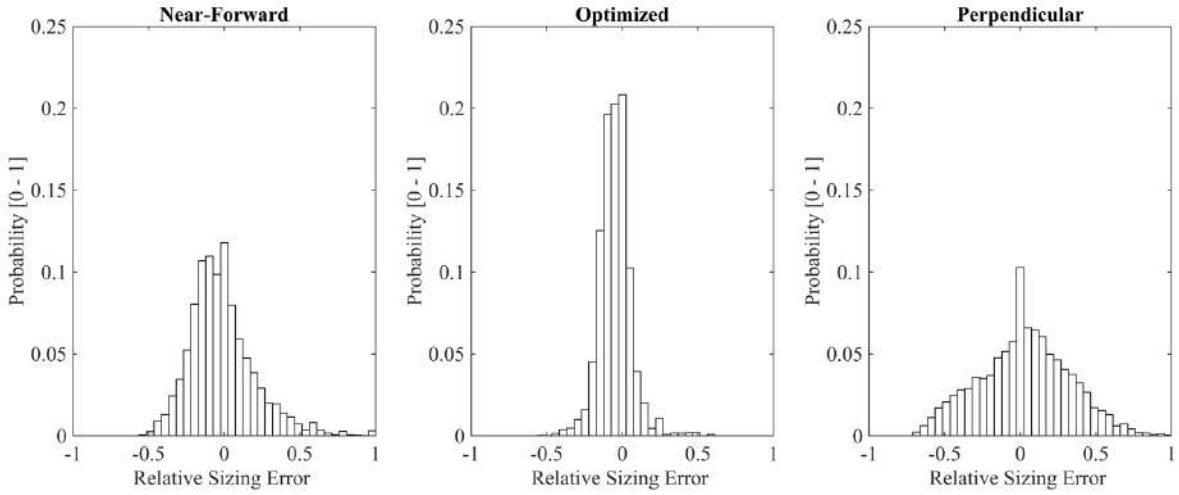

Figure 6: Simulated RSE for absorbing particles in the range 0.1 to 10um.

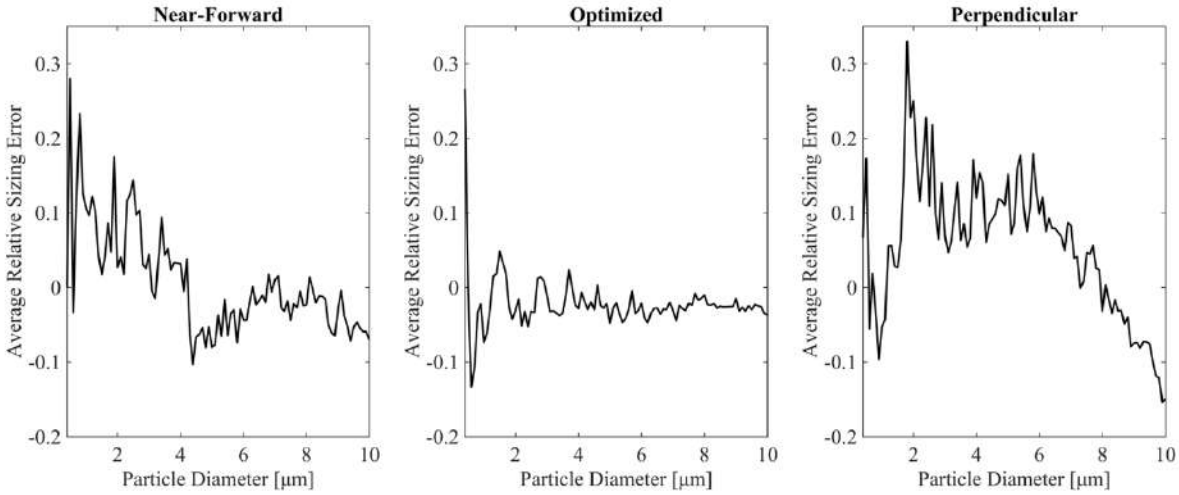

Figure 7: Average simulated RSE as a function of particle diameter for non-absorbing particles.

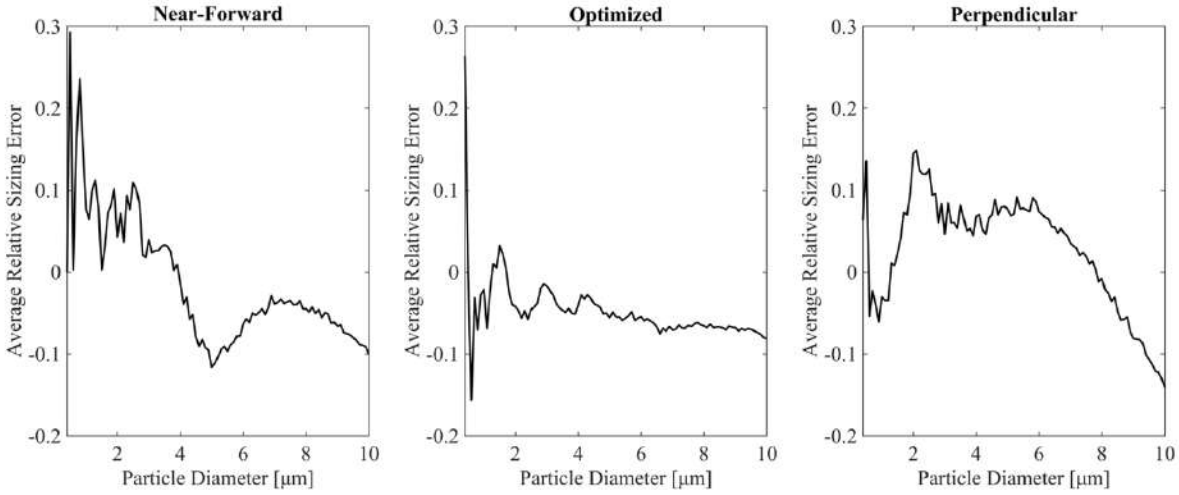

Figure 8: Average simulated RSE as a function of particle diameter for absorbing particles.

CHAPTER 3: EXPERIMENTAL SETUP

3.1 OPTICAL CELL DESIGN

To evaluate the validity of the numerical findings and to test the performance of the optimal angular range in comparison to the other two, an experimental setup was built. Figure 9 shows a diagram of the setup. The optical cell is positioned inside the 300mm x 300mm x 250mm hermetically sealed enclosure, where the interior is painted with non-reflective matte black paint. The enclosure is placed on an optical table to allow for precision adjustments of the angular range used for light collection. The test particles are aerosolized from an aqueous solution in an aerosol nebulizer (In-Tox Lovelace Aerosol Nebulizer) mixed with clean and dry air in a heated mixing chamber before traveling through a Nafion membrane dryer that reduced the moisture of the aerosol mix. Out of the membrane dryer, the aerosol mix goes into a particle chamber where the pressure is atmospheric.

The enclosure was placed between the particle chamber and a TSI Aerodynamic Particle Sizer (TSI APS, Model 3310), where the APS sampling pump aspirated air laden with size controlled particles at a rate of 1 lpm. The APS was used as a reference and to monitor that only monodisperse particles of the correct size were present in the system during each experiment. The following monodisperse spherical particles were used in the experiments: 2 and 4 μm PSL with a CRI of 1.61-0i (Thermo-Fisher), 2 and 4 μm silica with a CRI of 1.53-0i (Cospheric), and 2 and 4 μm alumina with a CRI of 1.78-0i (Corpuscular).

Figure 9B shows a diagram of the optical cell used for testing. Despite the experimental setup being constructed on an optical table and relying on large auxiliary equipment, the optical cell is designed as a compact low-cost device. This allows for a short turnaround in moving from a highly

adjustable setup to a final realized device. The optical cell uses exclusively components that are chosen for their low cost and compactness. The incident light source is a 120mW laser diode (Osram PL450B) that emits a blue laser beam at 450nm and 70mW (running below maximum power for increased durability and stability). The laser diode has a small form factor measuring 3.2 mm in diameter. The laser beam is linearly polarized and focused using a 6mm lens into an elliptical point where the particle jet stream intersects the laser beam. The intensity profile of the focused laser beam is approximately Gaussian. The laser beam passes through two rectangular apertures to minimize stray light and to shape the final beam before it traverses the collimated particle stream. The elliptically shaped laser beam measures approximately 0.5x2mm in diameter, with the longer axis angled perpendicular to the particle flow. The laser beam is trapped in a custom laser beam dump that uses an absorptive neutral density filter (OD = 3.0) to absorb a large portion of the light and reflect the rest into a geometrical trap. The particle stream inlet is a 1.8mm (ID) hypodermic stainless steel tube and the outlet uses a 3mm (ID) tube, the distance between the two is 5mm. No sheath flow is present to minimize the size and complexity of the design. The intersection of the particle stream and the laser beam creates a cylindrical optical volume with a diameter of 1.8mm and length of 1mm. The photodetector is a photodiode with a 3.2mm square active area positioned to collect the scattered light at an adjustable angle. The main advantages of this optical cell design are simplicity, adjustability, and flexibility that allows to test multiple angular ranges and components, adjust the number of sizing bins, the integration time and to test sizing algorithms with short a turnaround in the design cycles. In this work we tested a relatively simple geometry: the absence of mirrors and collection optics results in a simple design that can be manufactured easily, remains durable and comes in a small form factor, with minimum need

for alignment and recalibration. The total cost of components is under $100 and all the components are designed to be used in the final device.

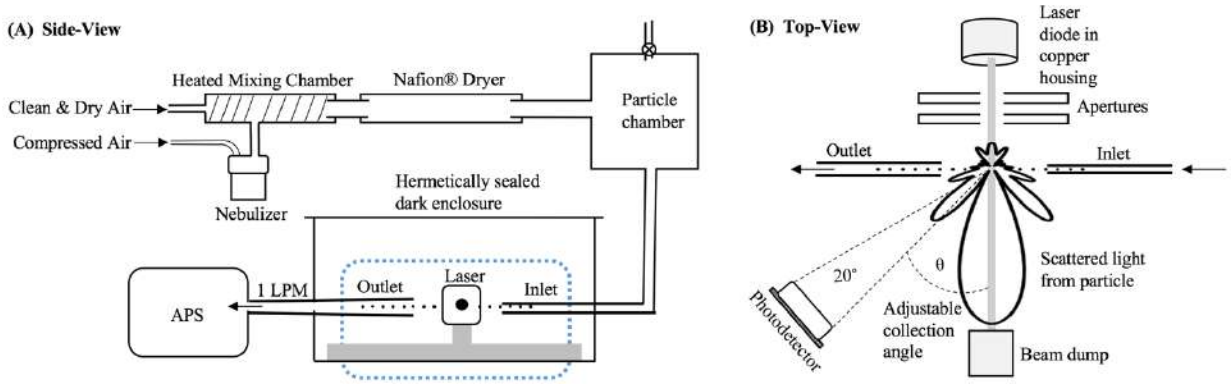

Figure 9: (A) Diagram showing the experimental setup. (B) Top-view of the optical volume in the experimental setup, marked by a blue region on (A).

3.2 SIGNAL PROCESSING & PERFORMANCE ESTIMATES

The following calculations are meant to estimate the expected performance of the OPC, all calculations are based on the optimal range (38-58°). When a particle traverses the Gaussian intensity profile of the laser beam, it scatters light in all directions, and a portion of the light is detected by the photodiode. The photodiode output is a Gaussian shaped pulse which is amplified using a two stage trans-impedance amplifier with active filtering. The signal is processed in an Atmel AVR microcontroller with a built-in analog to digital converter, modified to enable a sampling rate of 52 kHz and a 10-bit analog to digital resolution in the range from 0 to 1 V. The microcontroller uses an adaptive peak detection algorithm to find the amplitude of the Gaussian shaped pulse, and subsequently it sorts the amplitude into bins corresponding to the size of the particle. Figure 10 shows a pulse from a 2 μm spherical PSL particle measured using the experimental setup.

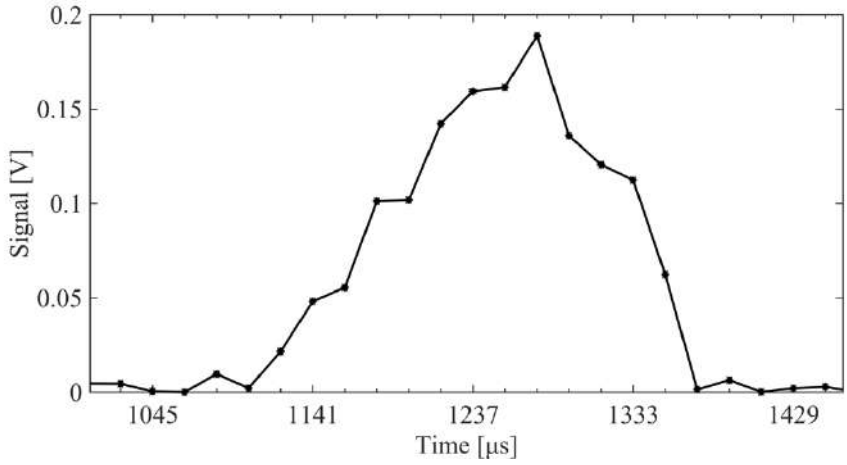

Figure 10: A Gaussian-shaped pulse for a 2 μm PSL particle. The pulse was measured using the experimental setup. The x-axis shows the time in μs where each minor tick is 19.23 μs. The y-axis shows the amplified voltage from the photodiode.

The optical cell uses a 1.8 mm (ID) particle inlet for the 1 lpm aerosol flow which translates into an average air velocity of approximately 6.5 m/s. A particle traveling at that velocity crosses the 1mm long optical volume in 76.9 μs. The microcontroller samples at 52kHz, resulting in an average of 4 samples for each particle that travels through the optical volume. However, as observed in Figure 10, the realized particle velocity is much slower than 6.5 m/s. Based on the flow and sampling rate of the device, the theoretical maximum particle concentration that the device is capable of measuring is 6500 particles per second. The targeted size range for detectable ambient particles is 0.3 to 10 μm, particles smaller than 0.3 μm are difficult to detect without the use of a more sensitive photodetector, such as a photomultiplier tube. With the design parameters set, the theoretical performance can be estimated using Mie theory. The laser diode is set to 70mW and the resulting elliptical laser beam has a power density of 7 Wcm^{-2}. The scattering cross section of a 0.3 μm spherical PSL particle with a CRI of 1.61-0i is $1.857 \cdot 10^{-9}$ cm^2 according to Mie theory and 3.7% of the scattered light is collected onto the photodiode. The responsivity of the photodiode for 450 nm light is 0.21 A/W and after amplifying the signal, the resulting voltage pulse is 10.5

mV. The LOD in OPCs is commonly defined as a S/N of at least 10, where S/N is defined as the ratio of the detected signal peak amplitude to the standard deviation of the background noise. The microcontroller resolution is 1 mV, hence the design is theoretically sensitive enough to detect 0.3 μm particles if the background noise is very limited. Based on the same methodology, the resulting voltage pulse from a 10 μm particle is 687 mV which is inside the dynamic range of the electronics. The upper limit of the dynamic range, 1000mV, corresponds to a 16 μm particle rendering the theoretical particle size range of the device to be approximately 0.3 to 16 μm, which is larger than expected. This can be attributed to the location of the optimized angular range; it is located so that the dynamic range required is limited. As the particle size increases, the scattered light gets more focused to the forward direction and with the optimized angular range located in the semi-forward direction, the percentage of light collected decreases as the particle size increases, allowing for a manageable dynamic range. When a 10 μm particle is detected, only 0.36% of the light is collected compared to 3.6% for 0.3 μm particles.

CHAPTER 4: RESULTS AND DISCUSSION

The optimization scheme considered all possible angular ranges in order to determine the optimal one, the numerical analysis included the optimal angular range in addition to two alternatives. In the experimental study, we test the system's response for the same three distinct angular ranges, the optimized range (38-58°), the perpendicular range (80-100°) and near-forward range (5-25°). All three angular ranges are equally sized and the experiments were performed using the same adjustable setup. For each angular range, the system's response was first calibrated using monodisperse PSL spheres of 2 μm and 4 μm and subsequently used to count and size spherical monodisperse particles of the same two sizes, but for different CRIs, namely silica and alumina particles. The PSL particles had a CRI of 1.61-0i, the silica particles 1.53-0i, and the alumina particles 1.78-0i. This mimics the real world scenarios where the particles being measured come from diverse sources and have an unknown CRI while the device is calibrated for one specific CRI. The experiments were performed for each combination of angular range, particle size, and particle CRI; a total of 18 combinations. Each experiment was run until one thousand particles had been counted and sized; resulting in 18 datasets with one thousand data points each.

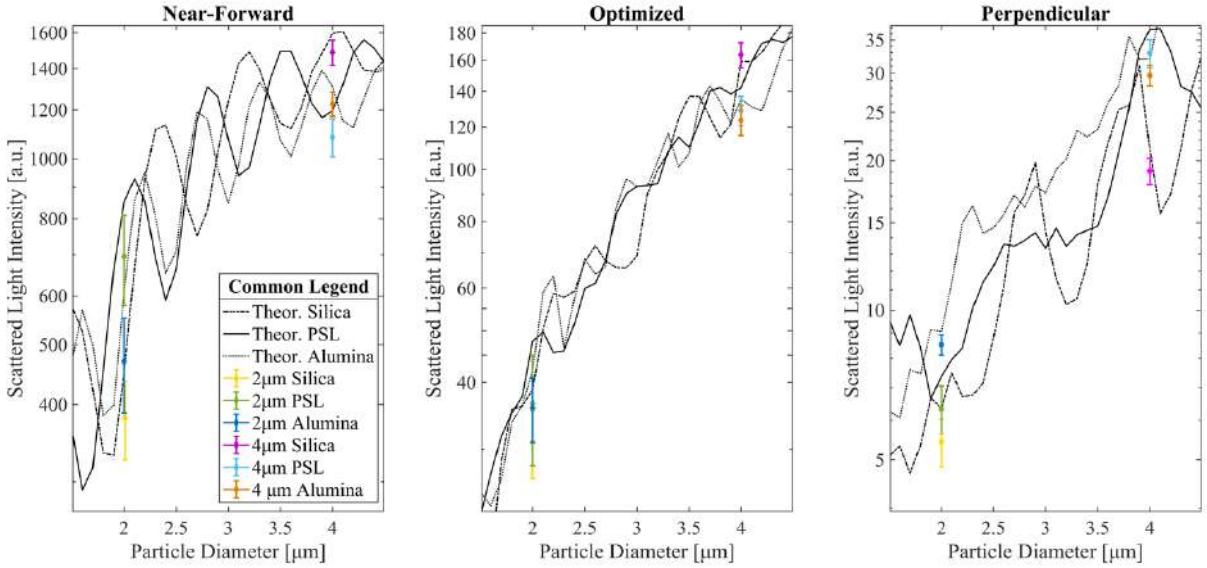

Figure 11: Comparison of theoretical and (uncalibrated) experimental scattered light intensity for all three angular ranges. Each experimental range is displayed as a marker (mean) with error bars extending to one standard deviation from the mean. The experiments include 2 and 4 µm monodisperse particles of silica, PSL, and alumina.

Figure 11 shows the experimental scattered light intensity in comparison to the theoretical scattered light intensity curves, the latter calculated with Mie theory. The experimental scattered light intensity is calculated from the uncalibrated raw datasets. The experimental scattered light intensity is displayed as a marker (the mean) with error bars extending to one standard deviation from the mean. The experimental data fits the theoretical curves adequately. However, there is a small systematic tendency of the experimental values being lower than the theoretical curves. Figure 12 displays the calibrated datasets as signal voltage in a histogram form, highlighting the distributions of the individual datasets. The distributions tend to have longer tails on the left while there is a sharper decline on the right. This is the same effect as observed previously in Figure 11, it is partially due to the Gaussian intensity profile of the laser beam. Particles that intersect the laser beam below or above the middle experience a lower incident light intensity compared to

particles that cross the laser beam in the middle. This effect is well documented [21] and can be avoided by focusing the laser beam into a uniform line using a cylindrical focusing lens, or by collimating the particle stream more tightly; both options that weren't considered for this device due to cost.

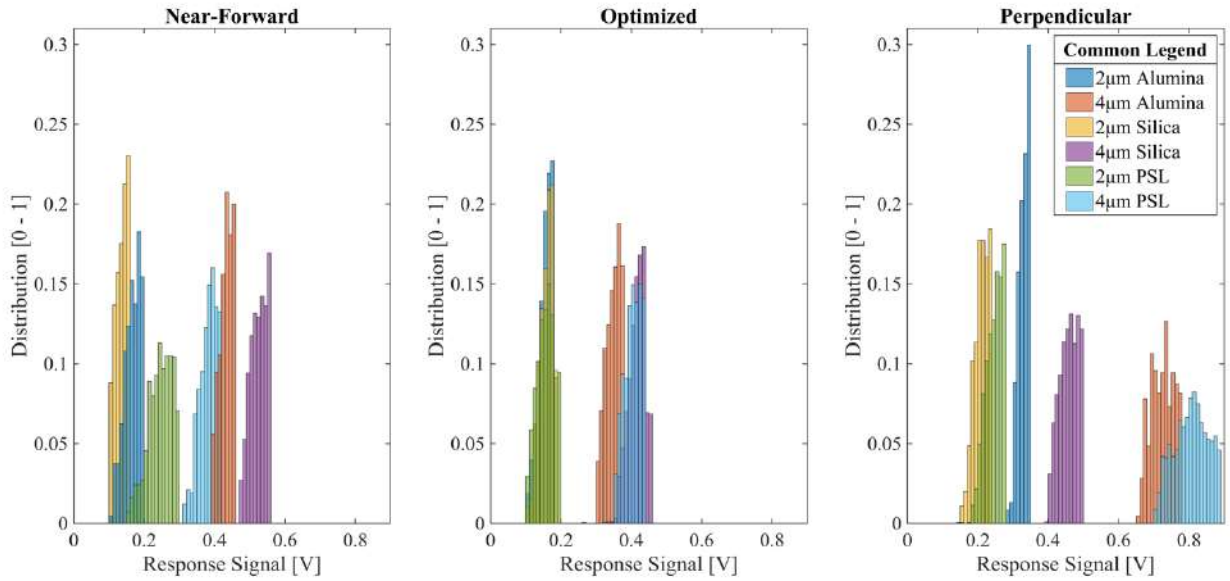

Figure 12: Experimental response signal distribution for near-forward, optimized and perpendicular angular ranges. The experiments include 2 and 4 μm monodisperse particles of silica, PSL, and alumina. Each dataset (color) is normalized so that the sum of the bars equals unity.

To assess the sizing performance (precision and accuracy) of each angular range, the RSE is computed from the experimental data. This is possible because the monodisperse particles tested are of a known size, and can be compared with the measured size from the experiments. Figures 13 through 15 show the individual RSE distributions for all three angular ranges. The width of each distribution indicates precision while its location (relative to the middle) represents the sizing accuracy. An ideal OPC with unique sizing capabilities and high precision would display tight individual distributions overlapping in the middle. The 2 and 4 μm PSL particles used for

calibration are colored in green and light blue respectively; they are understandably located in the middle in each figure. Figure 13 displays the experimental RSE for 2 μm monodisperse particles, where the device is calibrated to PSL but used to size silica, PSL, and alumina particles. The near-forward angular range has an RSE distribution with three distinct peaks, corresponding to the three particles tested, where silica and alumina particles are undersized. The optimized angular range has three overlapping RSE distributions, with tails extending towards RSE = -0.5. The perpendicular angular range has three distinct peaks in the RSE distribution, displaying undersizing of silica particles and oversizing of alumina particles. The experimental data shows that the optimized angular range is less sensitive to variations in the CRI of 2 μm monodisperse particles. However, the individual RSE distributions are the tightest, and tallest, for the perpendicular range. This is expected, the perpendicular angular range is conveniently located in the optical volume so that the effect of stray light is smaller than for the other two angular ranges, allowing for increased precision.

The RSE distribution for 4 μm monodisperse particles is displayed Figure 14 for all three angular ranges. The near-forward angular range oversizes both silica and alumina particles. The optimized angular range undersizes alumina particles and slightly oversizes silica particles. The perpendicular angular range undersizes both silica and alumina particles; the undersizing is more pronounced for the silica particles. In comparison to the 2 μm RSE distributions, all three angular ranges show tighter distributions for 4 μm particles. This is partially because RSE as a measure is relative to the size, 50% oversizing is not the same in μm for two different sizes.

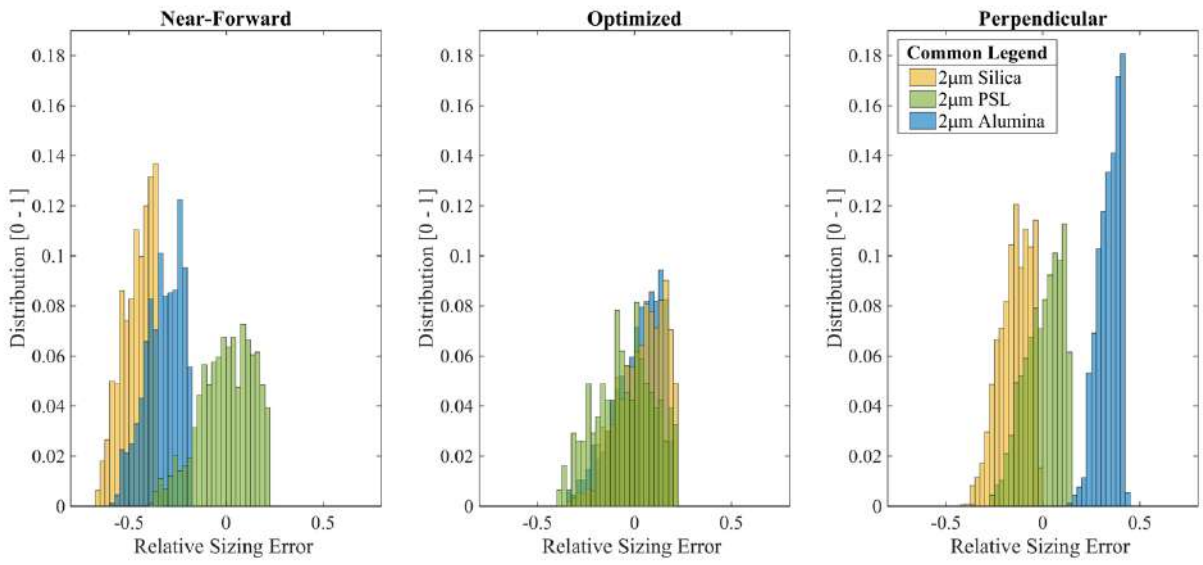

Figure 13: Experimental RSE distribution for near-forward, optimized and perpendicular angular range using monodisperse 2 µm particles of silica, PSL, and alumina. Each dataset (color) is normalized so that the sum of the bars equals unity.

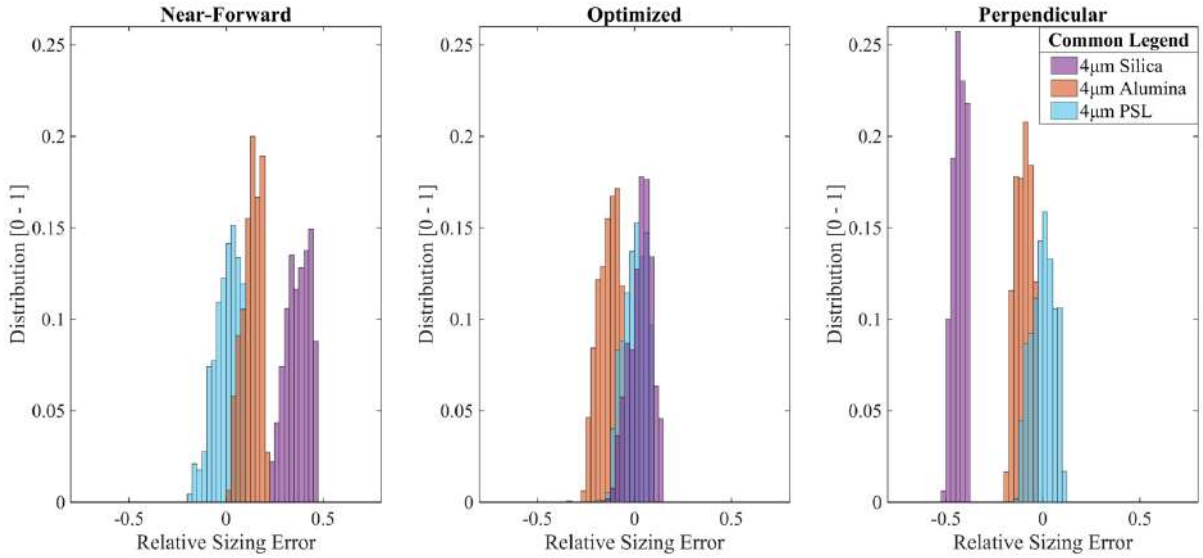

Figure 14: Experimental RSE distribution for near-forward, optimized and perpendicular angular range using monodisperse 4 µm particles of silica, PSL, and alumina. Each dataset (color) is normalized so that the sum of the bars equals unity.

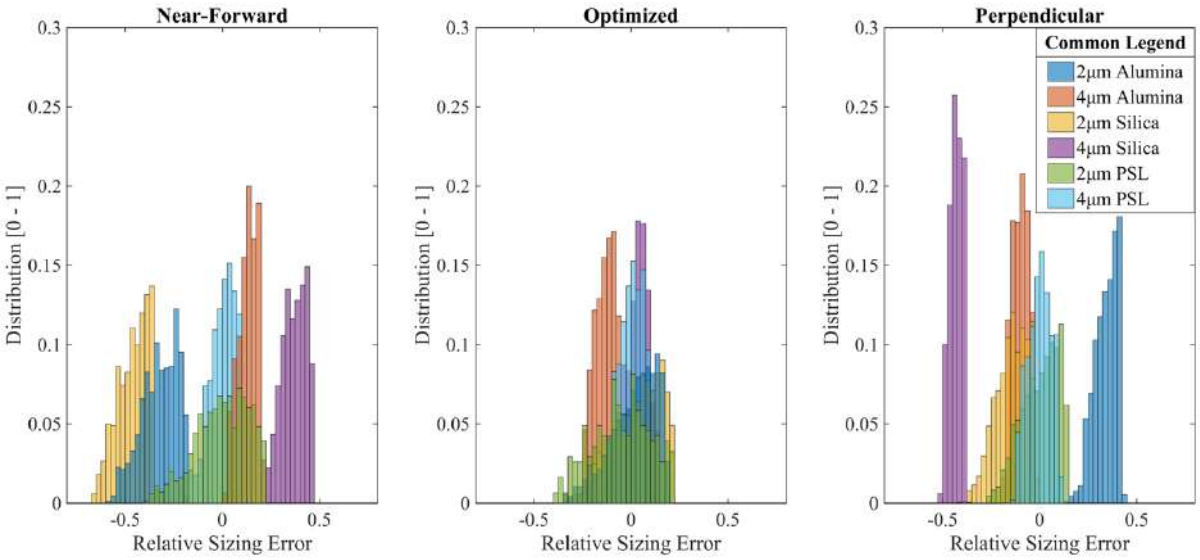

Figure 15: Experimental RSE distribution for near-forward, optimized and perpendicular angular range using 2 and 4 µm particles of silica, PSL, and alumina. Each dataset (color) is normalized so that the sum of the bars equals unity.

Figure 15 displays the overall RSE distributions for both 2 and 4 µm monodisperse particles. The perpendicular angular range has the bulk of the RSE distributions in the middle, with the exception of 2 µm alumina and 4 µm silica; outlying distributions that represent erroneous sizing due to CRI variations. The near-forward range is very sensitive to CRI variations; results that are somewhat inconsistent with previous studies. We suspect two parameters to be the main cause of this difference: stray light and the size of the angular range. Stray light rejection becomes increasingly difficult as the angular range moves closer to the direction of forward scattering. This experiment used the angular range 5-25° which is very close to the opposite direction of the incident laser beam; this angular range is essentially looking almost directly at the laser beam. Secondly, all three angular ranges in this experiment were equal in size, a decision made to ensure a fair basis for comparison. Previous studies often used very small angular ranges in the near-forward range, often only a few degrees in size, occupied by a photomultiplier tube instead of a photodiode. Using a

small angular range is not applicable in this study because the scattered light intensity would be insufficient for the low-cost photodiode. A generic small form factor photomultiplier tube costs around hundred times more than the photodiode used in this study.

Table 2 summarizes the results quantitatively. Overall, the optimized angular range is the least sensitive to CRI variations and is the most accurate when it comes to sizing particles of unknown CRI. The average absolute sizing error for the experiments is 32.21% for the near-forward angular range, 6.87% for the optimized angular range, and 25.45% for the perpendicular range. The perpendicular angular range was the most precise, with an average standard deviation of 6.07%, while the optimized and near-forward angular ranges had an average standard deviation of 8.93% and 7.93%.

Table 2: Statistics for the experimental datasets presented in Figure 15

		Perpendicular	Optimized	Near-Forward
2 μm Alumina	mean	0.3417	-0.0644	-0.3251
	stdev	0.0584	0.1108	0.0919
2 μm Silica	mean	-0.1451	-0.0417	-0.4614
	stdev	0.0803	0.1106	0.0774
2 μm PSL	mean	0	0	0
	stdev	0.0953	0.1493	0.1358
4 μm Alumina	mean	-0.1001	-0.1370	0.1307
	stdev	0.0396	0.0506	0.0470
4 μm Silica	mean	-0.4309	0.0318	0.3712
	stdev	0.0320	0.0578	0.0599
4 μm PSL	mean	0	0	0
	stdev	0.0584	0.0569	0.0640
Overall absolute	mean	0.2545	0.0687	0.3221
	stdev	0.0607	0.0893	0.0793

CHAPTER 5: CONCLUSIONS

This contribution described the process of optimizing and designing a compact low-cost optical particle counter for size measurements of aerosols. The angular range for collection of scattered light was optimized using a numerical model based on the elastic scattering of spherical homogeneous particles. The goal of the optimization was to find an angular range that minimized four characteristics, unfavorable to sizing accuracy. Namely, sensitivity to variations in the CRI of particles, non-monotonicity, and multivaluedness in the response function, dynamic range, and LOD. The optimized angular range was determined to be 38-58° relative to the incident laser beam. An experimental setup was used to validate the numerical findings and to test the performance of the optimized angular range in comparison to other two equally sized angular ranges, commonly employed in commercially available low-cost OPCs. The adjustable experimental setup used small form factor low-cost components, designed and intended for the realized device. The experiments used six different aqueous solutions of spherical monodisperse particles of known size and CRI; PSL (n = 1.61), alumina (n = 1.78), and silica (n = 1.53); 2 and 4 μm in diameter. The PSL particles were used to calibrate the device before it was used to measure and size the alumina and silica particles. The experiments were meant to mimic real-world scenarios where the particles being measured come from diverse sources and do not have optical properties identical to the calibration particles.

The experimental response was in good agreement with the numerical calculations for all three angular ranges tested. An RSE analysis of the experimental results showed that the optimal angular range was the least sensitive to variations in CRI of particles, and overall the most accurate in terms of sizing. The perpendicular angular range was less accurate but slightly more precise. The near-forward angular range was the least accurate, displaying high sensitivity to CRI variations.

The findings were consistent across the two sizes and all CRIs. The average absolute sizing error was 32.21% for the near-forward angular range, 6.87% for the optimized angular range, and 25.45% for the perpendicular range. The perpendicular angular range was the most precise, with an average standard deviation of 6.07%, while the optimized and near-forward angular ranges had an average standard deviation of 8.93% and 7.93%.

The results show clearly that the optimal angular range is effective in eliminating the ambiguity that is commonly present when OPCs are used in the field. The decision to use low-cost components throughout the process was a vital part of the design philosophy. The components used in the experimental setup are now being combined into a compact sensor for further evaluation and field testing.

REFERENCES

1. Beelen, R., et al., *Long-Term Effects of Traffic-Related Air Pollution on Mortality in a Dutch Cohort (NLCS-AIR Study).* Environmental Health Perspectives, 2008. **116**(2): p. 196-202.
2. Krewski, D., et al., *Overview of the reanalysis of the Harvard Six Cities Study and American Cancer Society Study of Particulate Air Pollution and Mortality.* J Toxicol Environ Health A, 2003. **66**(16-19): p. 1507-51.
3. Krewski, D., et al., *Extended follow-up and spatial analysis of the American Cancer Society study linking particulate air pollution and mortality.* Res Rep Health Eff Inst, 2009(140): p. 5-114; discussion 115-36.
4. Pope, C.A., 3rd, et al., *Lung cancer, cardiopulmonary mortality, and long-term exposure to fine particulate air pollution.* Jama, 2002. **287**(9): p. 1132-41.
5. Pope, C.A., 3rd and D.W. Dockery, *Health effects of fine particulate air pollution: lines that connect.* J Air Waste Manag Assoc, 2006. **56**(6): p. 709-42.
6. Pope, C.A., 3rd, et al., *Particulate air pollution as a predictor of mortality in a prospective study of U.S. adults.* Am J Respir Crit Care Med, 1995. **151**(3 Pt 1): p. 669-74.
7. Samet, J.M., et al., *Fine particulate air pollution and mortality in 20 U.S. cities, 1987-1994.* N Engl J Med, 2000. **343**(24): p. 1742-9.
8. Lim, S.S., et al., *A comparative risk assessment of burden of disease and injury attributable to 67 risk factors and risk factor clusters in 21 regions, a systematic analysis for the Global Burden of Disease Study 2010.* The Lancet, 2012. **380**(9859): p. 2224-2260.
9. Brown, J.S., K.L. Zeman, and W.D. Bennett, *Ultrafine particle deposition and clearance in the healthy and obstructed lung.* Am J Respir Crit Care Med, 2002. **166**(9): p. 1240-7.
10. Schwartz, J. and L.M. Neas, *Fine Particles Are More Strongly Associated Than Coarse Particles with Acute Respiratory Health Effects in Schoolchildren.* Epidemiology, 2000. **11**(1): p. 6-10.
11. Elbayoumi, M., N.A. Ramli, and N.F.F. Md Yusof, *Spatial and temporal variations in particulate matter concentrations in twelve schools environment in urban and overpopulated camps landscape.* Building and Environment, 2015. **90**: p. 157-167.

12. Patel, M.M., et al., *Spatial and Temporal Variations in Traffic-related Particulate Matter at New York City High Schools.* Atmospheric environment (Oxford, England : 1994), 2009. **43**(32): p. 4975-4981.
13. European Parliament. *Directive 2008/50/EC of the European Parliament and of the Council of 21 May 2008 on ambient air quality and cleaner air for Europe*, in *152*, EU, Editor. 2008, Official J. p. 1-44.
14. EPA, *40 CFR Parts 50 - Reference Methods for the Determination of Fine Particulate Matter as PM2.5 in the Atmosphere (Appendix L)*, EPA, Editor. 1997a.
15. Cohen, A.J., et al., *Urban air pollution.* Comparative quantification of health risks: global and regional burden of disease attributable to selected major risk factors, 2004. **2**: p. 1353-1433.
16. EPA, *40 CFR Parts 50 - Reference Methods for the Determination of Coarse Particulate Matter as PM10-2.5 in the Atmosphere (Appendix O)*, EPA, Editor. 1997b.
17. Gao, M., J. Cao, and E. Seto, *A distributed network of low-cost continuous reading sensors to measure spatiotemporal variations of PM2.5 in Xi'an, China.* Environmental Pollution, 2015. **199**: p. 56-65.
18. Sousan, S., et al., *Inter-comparison of low-cost sensors for measuring the mass concentration of occupational aerosols.* Aerosol Science and Technology, 2016. **50**(5): p. 462-473.
19. Wang, Y., et al., *Laboratory Evaluation and Calibration of Three Low-Cost Particle Sensors for Particulate Matter Measurement.* Aerosol Science and Technology, 2015. **49**(11): p. 1063-1077.
20. Austin, E., et al., *Laboratory Evaluation of the Shinyei PPD42NS Low-Cost Particulate Matter Sensor.* PLOS ONE, 2015. **10**(9): p. e0137789.
21. Renard, J.B., et al., *LOAC: a small aerosol optical counter/sizer for ground-based and balloon measurements of the size distribution and nature of atmospheric particles – Part 1: Principle of measurements and instrument evaluation.* Atmos. Meas. Tech., 2016. **9**(4): p. 1721-1742.
22. Nagy, A., et al., *Numerical and experimental study of the performance of the dual wavelength optical particle spectrometer (DWOPS).* Journal of Aerosol Science, 2007. **38**(4): p. 467-478.

23. Bohren, C.F. and D.R. Huffman, *Absorption and scattering of light by small particles*. 1983, New York: Wiley. xiv, 530 pages.
24. Mie, G., *Beiträge zur Optik trüber Medien, speziell kolloidaler Metallösungen.* Annalen der Physik, 1908. **330**(3): p. 377-445.
25. Jean-Baptiste, R., et al., *Small-angle light scattering by airborne particulates: Environnement S.A. continuous particulate monitor.* Measurement Science and Technology, 2010. **21**(8): p. 085901.
26. Shettle, E.P. and R.W. Fenn, *Models for the Aerosols of the Lower Atmosphere and the Effects of Humidity Variations on Their Optical Properties.* AFGL-TR-79-0214, 1979. **675**: p. 94.
27. Raut, J.C. and P. Chazette, *Vertical profiles of urban aerosol complex refractive index in the frame of ESQUIF airborne measurements.* Atmos. Chem. Phys., 2008. **8**(4): p. 901-919.
28. Ebert, M., et al., *The chemical composition and complex refractive index of rural and urban influenced aerosols determined by individual particle analysis.* Atmospheric Environment, 2004. **38**(38): p. 6531-6545.

APPENDIX A - MIE THEORY

The elastic scattering of light by spherical particles is fully characterized by Mie theory, or more specifically by the Mie solution to the Maxwell equations. The mathematical basis of the Mie solution and the methodology used in coding an efficient "Mie code" is the subject of this Appendix, explicit expressions for angle dependent scattering functions are derived with a reference to the code in Appendix B. All derivations and calculations are based on the great book by Bohren and Huffman [23]. The Mie solution is an exact solution that quantifies the scattering and absorption of an electromagnetic plane wave by spherical particles of an arbitrary diameter and refractive index. The solution is valid in situations where the diameter of the particle is comparable to the wavelength of the incident light. An electromagnetic field in a linear, isotropic, homogenous medium must satisfy the wave equation

$$\nabla^2 E + k^2 E = 0 \tag{A.1}$$

$$\nabla^2 B + k^2 B = 0 \tag{A.2}$$

Where E and B represent the electric and magnetic fields and k is the wavenumber. Accounting for the fact that both equations are divergence free and using the obvious symmetry that a sphere offers, this pair of vector equations can be reduced down to a problem of solving a single scalar wave equation in spherical coordinates (r, θ, ϕ).

$$\frac{1}{r^2}\frac{\partial}{\partial r}\left(r^2 \frac{\partial \psi}{\partial r}\right) + \frac{1}{r^2 \sin\theta}\frac{\partial}{\partial \theta}\left(\sin\theta \frac{\partial \psi}{\partial \theta}\right) + \frac{1}{r^2 \sin\theta}\frac{\partial^2 \psi}{\partial \phi^2} + k^2 \psi = 0 \tag{A.3}$$

Where ψ is a generating function that satisfies the wave equation in spherical coordinates. Hence, we seek a particular solution on the form $\psi(r,\theta,\phi) = R(r)\Theta(\theta)\Phi(\phi)$ and by combining that expression into Eq. (A.3) we arrive at the following expressions:

$$\frac{d^2\Phi}{d\phi^2} + m^2 = 0 \tag{A.4}$$

$$\frac{1}{\sin\theta}\frac{d}{d\theta}\left(\sin\theta\ \frac{d\Theta}{d\theta}\right) + \left(n(n+1) - \frac{m^2}{\sin^2\theta}\right)\Theta = 0 \tag{A.5}$$

$$\frac{d}{dr}r^2\frac{dR}{dr} + \left(k^2r^2 - n(n+1)\right)R = 0 \tag{A.6}$$

Where m and n are constants that ψ must satisfy. We are exclusively looking at electromagnetic wave scattering outside spherical particles. Assuming that the incident electromagnetic wave is naturally polarized (i.e. unpolarized) the scattering intensity, I, at an angle θ measured from the direction of the incident beam (i.e $\theta = 0°$ is pure forward scattering and $\theta = 180°$ is pure backscattering) can be fully described with the following infinite series expression:

$$I(\cos\theta) = \frac{|S_1(\cos\theta)|^2 + |S_2(\cos\theta)|^2}{2} \tag{A.7}$$

where:

$$S_1(\cos\theta) = \sum_{n=1}^{\infty}\frac{2n+1}{n(n+1)}(a_n\pi_n + b_n\tau_n) \tag{A.8}$$

$$S_2(\cos\theta) = \sum_{n=1}^{\infty}\frac{2n+1}{n(n+1)}(b_n\pi_n + a_n\tau_n) \tag{A.9}$$

Using the following values initially for τ and π:

$$\pi_0 = 0$$

$$\pi_1 = 1$$

$$\pi_2 = 3\cos\theta$$

$$\tau_0 = 0$$

$$\tau_1 = \cos\theta$$

$$\tau_2 = 3\cos 2\theta$$

and the recurrance relations:

$$\pi_n = \frac{2n-1}{n-1}\cos\theta\ \pi_{n-1} - \frac{n}{n-1}\pi_{n-2} \tag{A.10}$$

$$\tau_n = n\cos\theta\ \pi_n - (n+1)\pi_{n-1} \tag{A.11}$$

The two constants a_n and b_n are expressed as follows:

$$a_n = \frac{\mu m^2 j_n(mx)\left(x\, j_n(x)\right)' - \mu_1 j_n(x)(mx j_n(mx))'}{\mu m^2 j_n(mx)\left(x h_n^{(1)}(x)\right)' - \mu_1 h_n^{(1)}(x)(mx j_n(mx))'} \tag{A.12}$$

$$b_n = \frac{\mu_1 j_n(mx)\left(x\, j_n(x)\right)' - \mu j_n(x)(mx j_n(mx))'}{\mu_1 j_n(mx)\left(x h_n^{(1)}(x)\right)' - \mu h_n^{(1)}(x)(mx j_n(mx))'} \tag{A.13}$$

Where m is the complex refractive index of the sphere relative to the ambient medium, $x = \frac{d\pi}{\lambda}$ where d is the diameter of the particle and λ the wavelength of the incident electromagnetic wave, $\mu_1$is the magnetic permeability of the particle and μ the magnetic permeability of the ambient medium, $j_n(s)$ are spherical Bessel functions of order $n = (1,2,3 \dots)$ and

$$h_n^{(1)}(s) = j_n(s) + iy_n(s)$$

are spherical Hankel functions (a linear combination of spherical Bessel functions) of order

$$n = (1,2,3 \dots),$$

prime notations represent the derivatives of the corresponding arguments. Additionally, the following relations are used for the spherical Bessel functions

$$j_n(s) = \sqrt{\frac{\pi}{2s}} J_{n+0.5}(s) \tag{A.14}$$

$$y_n(s) = \sqrt{\frac{\pi}{2s}} Y_{n+0.5}(s) \tag{A.15}$$

Where $J_n$and $Y_n$are Bessel functions of first and second order, respectively. The following initial values are used for the Bessel functions:

$$j_0(s) = \frac{\sin s}{s}$$

$$j_1(s) = \frac{\sin s}{s^2} - \frac{\cos s}{s}$$

$$y_0(s) = \frac{-\cos s}{s}$$

$$y_1(s) = \frac{-\cos s}{s^2} - \frac{\sin s}{s}$$

and after that the following recurrance formula is used

$$u_{n-1}(s) + u_{n+1}(s) = \frac{2n+1}{s} u_n(s) \tag{A.16}$$

where u_n is either $j_n or\ y_n$.

The calculations are implemented in Matlab (Version R2016a). The basic structure of the code allows the user to compute scattering intensities for thousands of different particles for all angles in a timely manner. Every effort was made to optimize the code for fast computation of multiple particle sizes and refractive indices. The single most computationally expensive part of the code is the computation of the Bessel functions and despite optimization efforts, the built in besselj.m and bessely.m remain as the bottlenecks of the code. The scattering intensity, Eq. (A.7), is calculated using two infinite series. In the code, these infinite series are truncated after a fixed number of steps to ensure convergence and to limit error. The value used is the one recommended by Bohren and Huffman.

$$n_{max} = x + 4x^{\frac{1}{3}} + 2 \tag{A.17}$$

Where x is the size parameter.

In order to demonstrate the effectiveness of the code a few tests are carried out as an example. First example: examining the scattering intensity of spherical sulfate aerosols (n=1.45-0i) over a range of five discrete particle sizes as a function of observation angle produces the following plot.

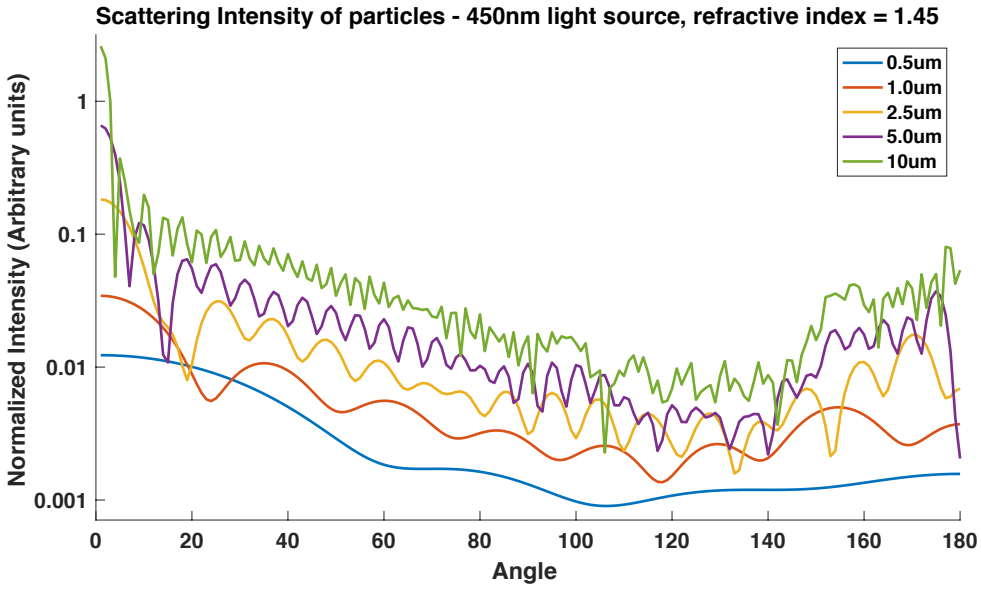

Second example: it is known that a variation in the refractive index of a particle of fixed size affects the scattering intensity differently depending on which angle is observed. Using spherical 1 μm particles as an example with refractive indices ranging from 1.3 to 1.7. The program produces the following plot.

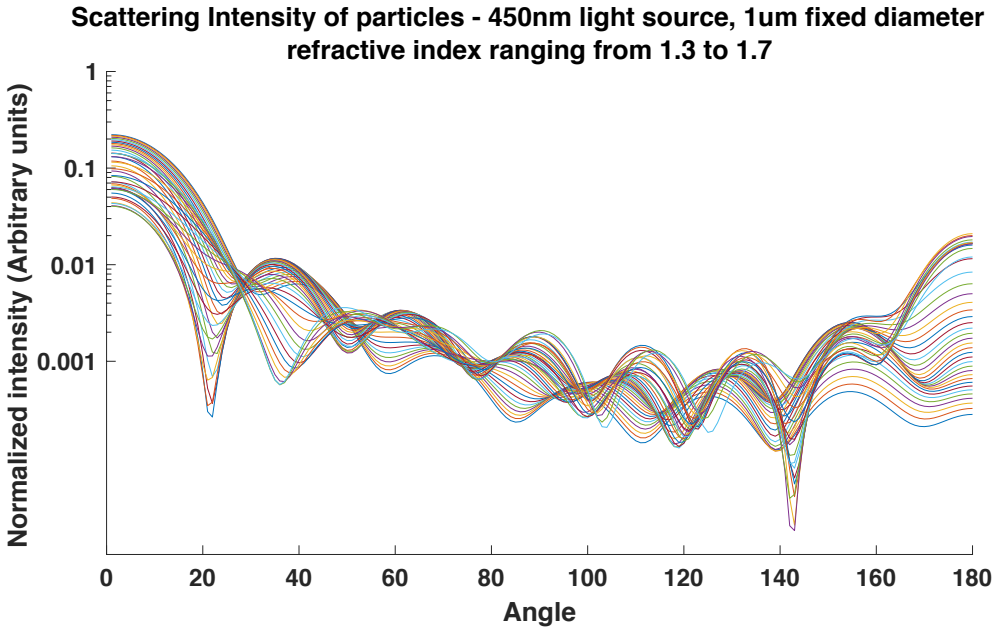
Scattering Intensity of particles - 450nm light source, 1um fixed diameter
refractive index ranging from 1.3 to 1.7
Normalized intensity (Arbitrary units)
1
0.1
0.01
0.001
0
20
40
60
80
100
120
140
160
180
Angle

APPENDIX B - ELECTRONICS

The following section describes the process of designing the photodiode amplification circuit. In our design, we knew that we had to amplify the signal from the photodiode with a gain of 20 million. We decided to use a trans impedance amplifier in the first stage, eliminating the need for a current to voltage converter to convert the very small current produced by the photodiode into voltage. Fortunately, the trans impedance amplifier is not technically amplifying the current, it is merely converting current to voltage with the use of the feedback resistor, which was chosen to be 470k. Because we are converting current to voltage with a gain of unity, the GBW product isn't affected as long as the feedback resistor is much smaller than the internal resistance of the photodiode which is on the scale of Giga Ohms. An unaffected GBW product essentially means that the system's response time is unaffected. This is exactly the reason why we employed a two stage amplifier. In contrast to the two-stage amplifier, we tested a single stage system with 20M gain over the single amplifier and the bandwidth deteriorated severely, as expected. The two-stage system is much better for this applications due to the very high gain (amplification) required. Instead of amplifying 20M over a single stage, we amplify 470K in the first stage and then 47 in the second stage, a total of approximately 20M. Additionally, the second operational amplifier gave us a perfect opportunity to implement an active high pass filter with a cutoff frequency at 500 Hz to cut out the stray light noise and general 60Hz line noise. Since most of the amplification is done in the trans impedance amplifier, we only need a gain of 47 in the non-inverting amplifier in the next stage so the bandwidth remains high, 300 kHz.

The photodiode system consists of two separate stages; the first stage is current to voltage converter, and the second stage is active high-pass filter with non-inverting amplifier. The photodiode will not be included in simulation because it needs various light conditions to operate,

which are difficult to simulate directly. Instead, the photodiode was replaced with current source, because it generates photocurrent when stimulated by light. In addition to the current source, a capacitor and resistor were also added in parallel to the current source. Figure C1 shows the example for the photodiode model.

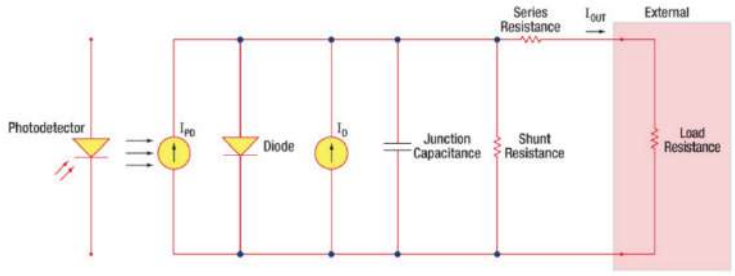

Figure C1: Schematic diagram of photodiode equivalent circuit for simulation.

The first stage of the circuit, the trans impedance amplifier is used as a current-to-voltage converter. It consists of one amplifier, a photodiode as the input, and a feedback resistor. As shown in Figure C2 the current to be amplified is applied to the inverting input. The circuit was designed to have the photodiode operate in photoconductive mode: exposure to light will cause a reverse current through the photodiode. If the reverse current through the photodiode is I_{ph}, then the output voltage is:

$$V_{out} = -I_{ph}R_f$$

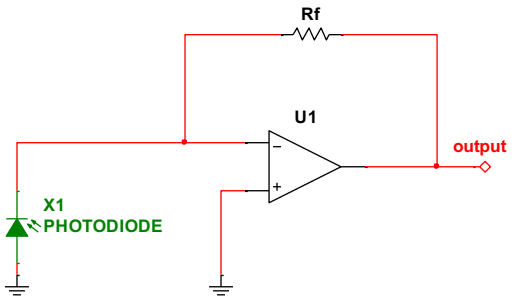

Figure C2: Basic op-amp trans impedance amplifier used as a current-to-voltage converter

Using the same concept as above, the circuit was built with R_f value of 470kΩ. The FDS100 photodiode produces an average of 6.5 nA current when light hits it, so a current source was placed to replace photodiode in simulation. The resulting voltage on the initial trans impedance amplifier was 24.0mV in this particular simulation. Thus the current has been converted to voltage and is now ready for more amplification.

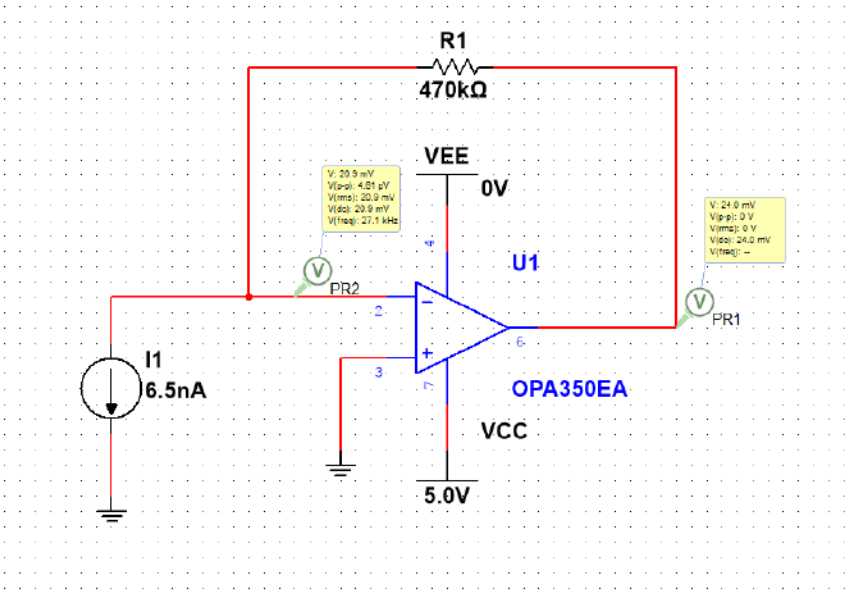

Figure C3: Current-to-voltage converter to amplified the current produce by the photodiode when it hits with light.

The second stage of the circuit is the active high-pass filter with non-inverting amplifier with a gain of 47. Figure C4 shows a resistor and capacitor pair that gives us a high pass filter with a cutoff frequency of 500 Hz to decrease noise. Since the value taken from the data sheet, 6.5 nA was the median current value, the output voltage we get is around 1V, but in the actual lab we were getting a square wave output with an amplitude of around 3-5V. The simulated version of the output of the second stage is shown in Figure C5. The bode plot of the active high pass filter also calculated during the simulation and shown in Figure C6.

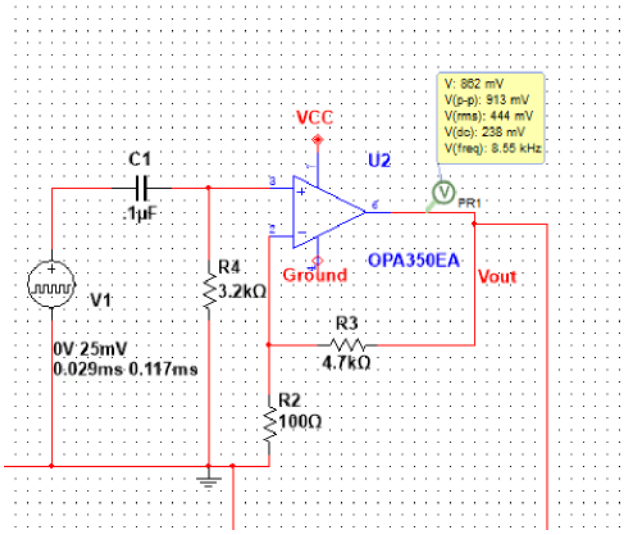

Figure C4: The second stage of the circuit. Active high-pass filter with non-inverting amplifier.

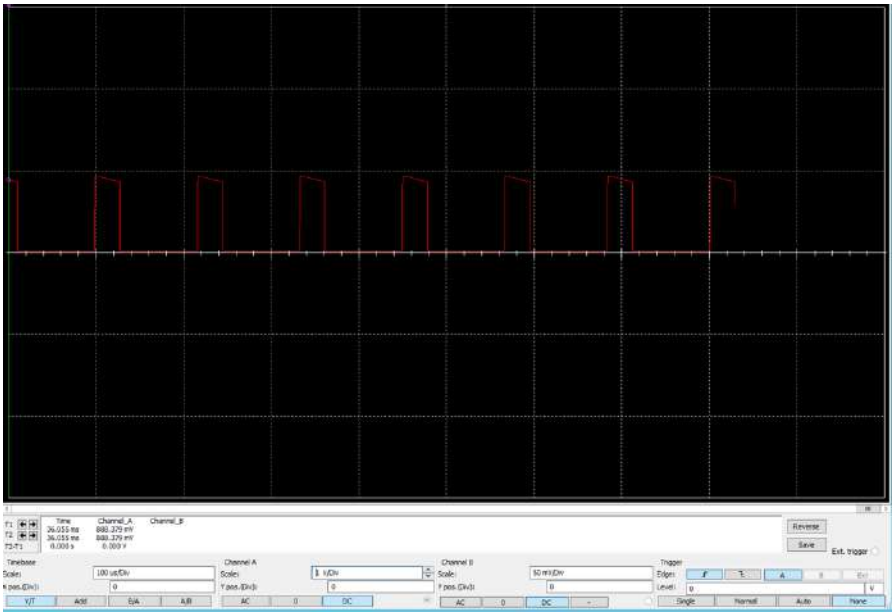

Figure C5: The simulated output of the second stage.

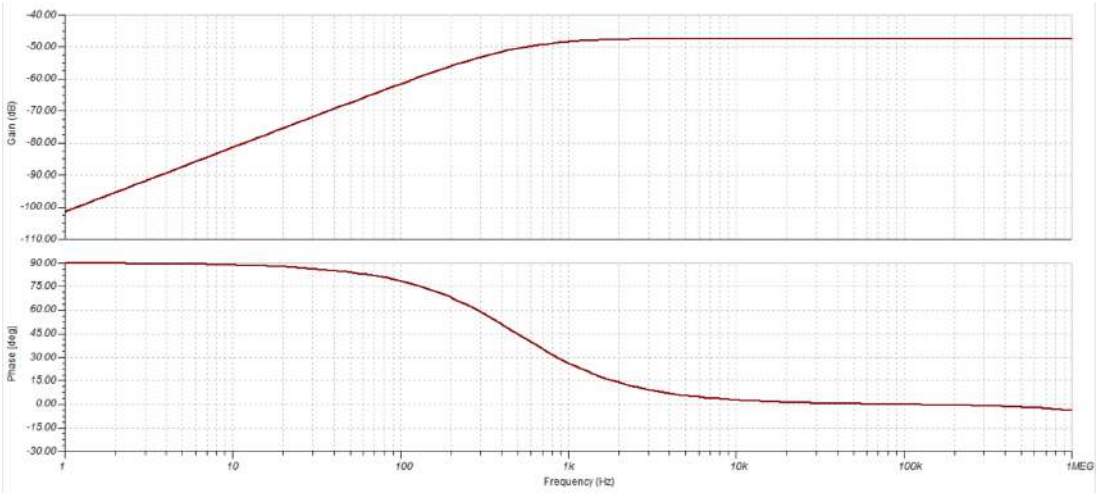

Figure C6: The bode-plot of the active high pass filter with amplification of the system.

After each stage of the system had been tested, the individual stages were combined with the current source as a replacement for the photodiode. Figure C7 shows an overview schematic of the entire photodiode amplifier circuit.

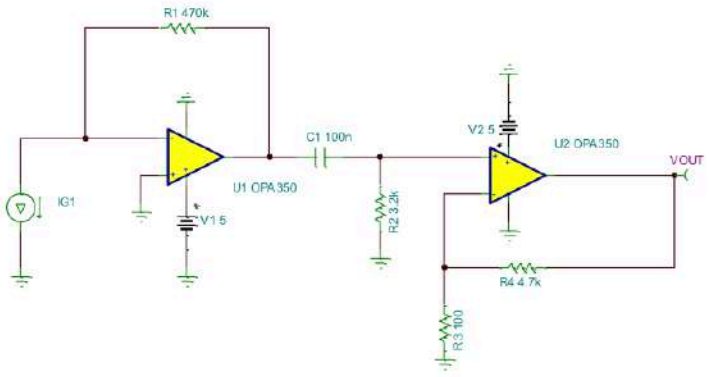

Figure C7: Overview of the full schematic of the photodiode amplifier circuit.

The last step of the project was to build the prototype of the circuit on a solderless prototyping breadboard. All the components used in the circuit were shown in Figure C7, and the current source was replaced by FDS100 Silicon photodiode. The test result of the circuit is shown in Figure C8, the circuit is clearly stable and responsive.

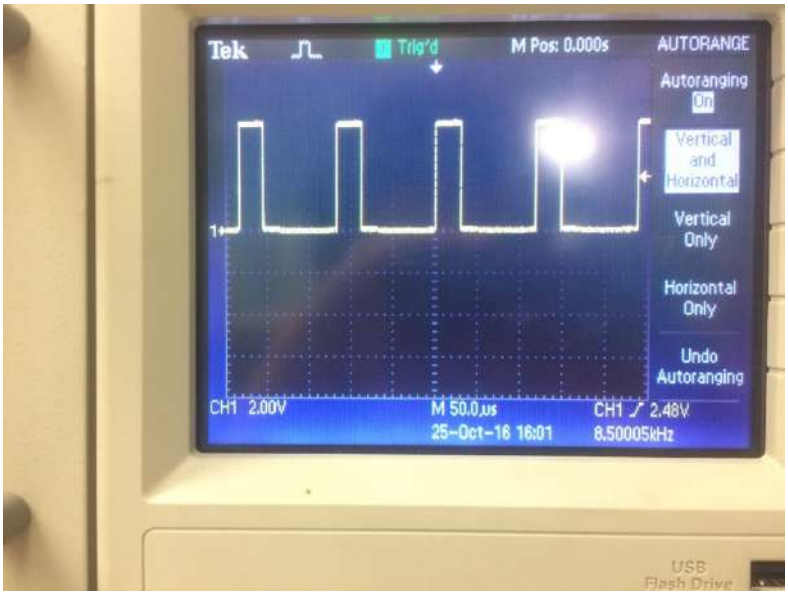

Figure C8: Output voltage of the system in a form of pulse waves, as a response to the light source provided from the LED.